Obtaining best estimates for the microphysical and radiative properties of tropical ice clouds from TWP-ICE in situ microphysical observations.

Alain Protat, Greg M. Mcfarquhar, J. Um, Julien Delanoë

Obtaining Best Estimates for the Microphysical and Radiative Properties of Tropical Ice Clouds from TWP-ICE In Situ Microphysical Observations

A. PROTAT

Centre for Australian and Weather and Climate Research, Melbourne, Australia, and Laboratoire Atmosphère, Milieux, et Observations Spatiales, Guyancourt, France

G. M. MCFARQUHAR AND J. UM

University of Illinois at Urbana–Champaign, Urbana, Illinois

J. DELANOË

University of Reading, Reading, United Kingdom

(Manuscript received 24 September 2009, in final form 10 September 2010)

ABSTRACT

Best estimates of the bulk microphysical and radiative properties (ice water content, visible extinction, effective radius, and total concentration) are derived for three case studies of tropical ice clouds sampled during the Tropical Warm Pool International Cloud Experiment (TWP-ICE). Two case studies are aged cirrus clouds produced by deep convection (the so-called 27/01 and 29/01 cases), and the third (''02/02'') is a fresh anvil produced by deep convective activity over the Tiwi Islands. Using crystal images obtained by a Cloud Particle Imager (CPI), it is observed that small ice particles (with maximum dimension $D < 50$–100 μm) were predominantly quasi spherical, with the degree of nonsphericity increasing rapidly in the $50 < D < 100$-μm range. For $D > 100$ μm, the aged cirrus clouds were predominantly characterized by bullet rosettes and aggregates of bullet rosettes, plates, and columns. In contrast, the fresh anvil had more frequent occurrences of plates, columns, aggregates of plates, and occasionally capped columns. The impact of shattering of large ice crystals on probe tips and the overall quality of the TWP-ICE in situ microphysical measurements are assessed. It is suggested that shattering has a relatively small impact on the CPI and cloud droplet probe (CDP) TWP-ICE data and a large impact on the Cloud Aerosol Spectrometer data, as already documented by others. It is also shown that the CPI size distributions must be multiplied by a factor of 4 to match those of the cloud imaging probe (CIP) for maximum dimension larger than 100 μm (taken as a reference). A technique [named Best Estimate of Area and Density (BEAD)] to minimize errors associated with the density (ρ)–D and projected area (A)–D assumptions in bulk microphysics calculation is introduced and applied to the TWP-ICE data. The method makes direct use of the frequency of occurrence of each particle habit as classified from the CPI data and prescribed ρ–D and A–D relationships from the literature. This approach produces ice water content (IWC) estimates that are virtually unbiased relative to bulk measures obtained from a counterflow spectrometer and impactor (CSI) probe. In contrast, the use of ρ–D and A–D relationships for single habits does produce large biases relative to the CSI observations: from −50% for bullet rosettes to +70%–80% for aggregates. The so-called width, length, area, and perimeter (WLAP) technique, which also makes use of individual CPI images, is found to produce positively biased IWCs (by 40% or so), and has a standard deviation of the errors similar to the BEAD technique. The impact of the large variability of the size distributions measured by different probe combinations on the bulk microphysical properties is characterized. The mean fractional differences with respect to the CSI measurements are small for the CPI + CIP, CPI, and CDP + CIP combinations (2.2%, −0.8%, and −1.1%, respectively), with standard deviations of the fractional differences ranging from 7% to 9%. This result provides an independent validation of the CPI scaling factor. The fractional differences produced between the CPI + CIP, CPI, and CDP + CIP combinations for extinction, effective radius, and total concentration are 33%, 10%–20%, and 90%, respectively, with relatively small standard deviations of 5%–8%. The fractional difference on total concentration varies greatly over the concentration range though, with values being larger than a factor of 2 for total concentrations smaller than 40 L^{-1}, but reducing to 10%–20% for concentrations larger than 100 L^{-1}. Therefore, caution should be exercised when using total concentrations smaller than 60–80 L^{-1} as references for radar–lidar retrieval evaluation.

Corresponding author address: Alain Protat, Centre for Australian Weather and Climate Research (CAWCR), 700 Collins St., Docklands, Melbourne, VIC 3008, Australia.
E-mail: alain.protat@latmos.ipsl.fr

DOI: 10.1175/2010JAMC2401.1

1. Introduction

The importance of clouds on climate through their direct effect on the Earth radiation budget and water cycle is well recognized. Clouds and their interaction with incoming and outgoing radiation remain the largest source of uncertainty among future climate projections produced by climate models (e.g., Bony et al. 2006; Dufresne and Bony 2008). The way clouds are represented in weather prediction models also significantly affects the quality of weather forecasts (e.g., Jakob 2002).

Among the different clouds forming in the troposphere, tropical ice clouds are of particular importance, owing to their extensive horizontal and vertical coverage and their long life time (e.g., Sassen et al. 2008). The quantification of the net large-scale radiative effect of tropical ice clouds is very difficult to achieve because of the competing impacts of these clouds. Tropical ice clouds reflect incoming light reducing the amount of solar radiation reaching the earth's surface. However, they also absorb the upwelling infrared radiation emitted by the surface and emit it at a lower temperature, thereby reducing the net amount of outgoing infrared radiation to space and heating the upper troposphere. As a result even the sign of the net radiative effect of tropical ice clouds is a matter of debate, both at the scale of a given cloud and of a climate model grid box.

To estimate this net radiative effect correctly, the morphological properties (cloud base, height, thickness, amount), the bulk microphysical and radiative properties (ice water content, effective radius, total concentration, fall velocity, single-scattering properties), and the heating rates and radiative fluxes induced by the presence of these tropical clouds must be accurately characterized (e.g., Mather et al. 2007). Ground-based continuous active and passive remote sensing (cloud radar, lidar, radiometers) observations such as those conducted in the framework of the U.S. Department of Energy Atmospheric Radiation Measurement Program (ARM; Stokes and Schwartz 1994) and new spaceborne combinations of the same instruments such as the A-Train (Stephens et al. 2002) are most relevant for the statistical characterization of tropical ice clouds because they are the only sets of observations potentially capable of describing the high-resolution vertical variability of the ice cloud properties. In addition, long time series of such observations are already available at a number of tropical sites. However, there is a crucial need for further development and evaluation of cloud retrieval techniques, as there are still knowledge gaps to be filled regarding tropical ice clouds. One major unsolved problem is quantifying the size distribution of small ice crystals (maximum crystal dimension D less than 50–100 μm). The development of retrieval techniques and their evaluation requires the use of reference measurements, such as those collected by airborne in situ microphysical probes. However, it is still to be demonstrated that the current generation of probes available can be used as references throughout the full particle size range. Recent studies have demonstrated that aircraft probes having a protruding shroud or inlet—such as the Cloud Aerosol Spectrometer (CAS), the Forward Scattering Spectrometer Probe (FSSP), and the two-dimensional cloud (2DC) probe—were prone to significant artificial increases of small ice crystal concentrations through the shattering of larger ice crystals (e.g., Korolev and Isaac 2005; Field et al. 2003, 2006; McFarquhar et al. 2007a; Heymsfield 2007). The overestimation of the bulk microphysical properties derived from the particle size distributions affected by shattering is presumably very large. For tropical cirrus and anvils sampled during the Tropical Warm Pool–International Cloud Experiment (TWP-ICE; May et al. 2008), McFarquhar et al. (2007a) suggested overestimates by a factor of at least 3 for total number concentration, a factor of 2 for extinction, and 50% for ice water content (IWC). These large uncertainties invalidate the use of these in situ measurements as references for the evaluation of active remote sensing retrievals.

Other well-known sources of uncertainties in bulk microphysical properties derived from particle size distribution measurements are the assumptions made in the calculations of the bulk microphysical parameters about the mass (m)–maximum crystal dimension D [or density (ρ)–D] and projected area (A)–D relationships (or more generally an assumption about the dominant particle habit in the sampled volume), the uncertainties arising from the sizing and projected area estimate of the very complex shapes of ice particles, and the uncertainties in the sampling volume of some of the in situ sensors (e.g., Heymsfield 2007).

In the present study, sensors mounted on the Scaled Composites *Proteus* aircraft during TWP-ICE are used to develop a semiobjective method to derive the bulk microphysical properties of the sampled tropical ice clouds and the associated uncertainties. The paper is organized as follows. The in situ sensors and the caveats associated with their use are described in section 2 followed by a description of the case studies used (section 3). A comparison of the different in situ sensors in their overlapping ranges is described in section 4 to highlight uncertainties and derive corrections for some of the sensors. A simple methodology using particle habit classifications from the Cloud Particle Imager (CPI) to reduce errors associated with the ρ–D and A–D assumptions in bulk microphysics calculations is discussed in section 5.

The impact of the variability of the particle size distributions measured by different probe combinations on the resulting bulk microphysical properties is then quantified in section 6. Additionally in section 6, the contribution of small ice crystals to these bulk microphysical properties is characterized. Conclusions are given in section 7.

2. The TWP-ICE in situ microphysical sensors and their caveats

During TWP-ICE, in situ measurements of anvils and cirrus clouds of various ages were collected by the Scaled Composites *Proteus* aircraft off Darwin, Northern Territory, Australia, between 21 January and 14 February 2006. As already discussed by May et al. (2008) and McFarquhar et al. (2007a), the *Proteus* was equipped with a CAS probe, sizing between 0.5 and 50 μm, a cloud droplet probe (CDP; 2–48 μm), and a cloud imaging probe (CIP; 25–1550 μm). High-resolution images of ice particles between 9 and 1500 μm were also obtained by the CPI, from which detailed particle habit classifications were derived (Um and McFarquhar 2007, 2009). Direct IWC measurements in the range from 10^{-3} to 1 g m^{-3} were made with the counterflow spectrometer and impactor (CSI) probe. The principle of these measurements is described in McFarquhar et al. (2007a) and is not repeated here.

There are at least three possible measurements of the particle size distributions $N(D)$ using combinations of these sensors: from the CAS + CIP, the CDP + CIP, and the CPI. However, there are caveats associated with each of these combinations. It must be first stated clearly that all these sensors, because they have tips or inlets, could potentially produce shattering of large ice crystals. However, although this has not been fully characterized yet, the design of the probe tips is expected to enhance or minimize this shattering effect. There is evidence that the protruding shroud on the CAS significantly enhances measured concentrations from the shattering of large crystals when there are significant amounts of ice particles with $D > 125$ μm (McFarquhar et al. 2007a; Heymsfield 2007; Jensen et al. 2009). Unfortunately, particle arrival times were not measured by the CDP during TWP-ICE, so there is no way of quantifying and minimizing the effects of shattering on the CDP [using, e.g., the technique proposed by Heymsfield (2007)]. But at least it has been documented that the shattering effect on the CDP probe was much smaller than for the CAS probe during TWP-ICE (McFarquhar et al. 2007a). The sample area of the CDP and the CAS is 0.25 mm^2. For an airspeed of 120 m s^{-1} and a sample area of 0.25 mm^2 the sample volume is 0.03 L s^{-1}, which for a 10-s average corresponds to a minimum detectable number concentration of 3.3 L^{-1}, or a minimum detectable $N(D)$ of 1.65 L^{-1} μm^{-1} for the 2-μm bin widths of the CDP.

The CIP probe is becoming a well-established probe in its measurement range (25–1550 μm) and has been used by several authors these last five years or so (e.g., Heymsfield et al. 2006; McFarquhar et al. 2007b; Jensen et al. 2009; Tian et al. 2010). Although the CIP probe nominally sizes particles with D from 25 μm, Korolev et al. (1998) showed that errors in the measurements of D for particles with $D < 100$ μm reach up to 85% because of the small number of photodiodes occulted. Also, as explained in Lawson et al. (2006), particles with D larger than 100 μm can be undersized because of slow time response and depth-of-field effects and counted as 25-, 50-, and 75-μm particles. Even though the Korolev (2007) sizing correction algorithm based on diffractions theory has been applied to the TWP-ICE CIP data, there are presumably larger uncertainties in the sizing of these small particles. Further, Baumgardner and Korolev (1997) and Strapp et al. (2001) reported that the sample volume of optical array probes depended on the size of the particle measured. Because the depth of field is highly uncertain for $D < 100$ μm, many previous studies have used optical array probes to derive concentrations of particles only with $D \geq 100$ μm (e.g., McFarquhar and Cober 2004; McFarquhar et al. 2007b). In this paper, following these earlier works, only data from the CIP for maximum diameters larger than 100 μm are considered as a reference measurement. The shattering of large ice crystals on the CIP probe tips might also amplify the concentrations of small ice crystals, especially those with $D < 100$ μm. These points are problematic because removal of the CIP data for $37.5 \leq D \leq 87.5$ μm leaves a gap between the largest CDP bin of 48 μm and the CIP bin of 100 μm. There is no easy way to evaluate the real value of these CIP measurements in this diameter range, which explains why it is not documented yet in the literature. Therefore, to evaluate qualitatively how inaccurate those measurements are before using them in the CD + CIP combination, the CIP data in the 50- and 75-μm D bins are compared in section 4 with the CPI data.

Although the CPI was originally developed to obtain high-resolution images of ice crystals, Connolly et al. (2007) and Mioche et al. (2010) recently suggested that the CPI might also be able to accurately measure size distributions given sufficiently large averaging times. The large averaging times are needed because the sample volume of the CPI at a true airspeed of 100 m s^{-1}, 3.72×10^{-4} m^3 s^{-1}, is a factor of 416 smaller than that of the CIP used during TWP-ICE. It is expected that this low sample volume will tend to yield underestimated concentrations of large crystals, given that these large crystals

are typically found in low concentration. The effect of this low sample volume on the microphysical and radiative properties has not been well documented in the literature so far. As with all probes in this study, shattering of the large ice particles might contaminate the CPI measurements. However, the magnitude of this contamination has not been documented yet. This point will be addressed in section 4. To derive size distributions from the CPI, the algorithm of Connolly et al. (2007) allows a determination of the distance of a particle from the CPI object plane and hence its depth of field. However, because their results are applicable only to the University of Manchester version-1 CPI and not to the version-2 CPI used during TWP-ICE, an unknown calibration factor (hereinafter referred to as scaling factor) needs to be determined in the present study to compute the CPI size distributions. There is especially large uncertainty in the scaling factor for crystals with $D < 150$ μm because the version-2 CPI is more sensitive to the detection of small particles than the version 1. This CPI scaling factor is estimated using the CIP for $D \geq 100$ μm in section 4. Because CIP data for $D \geq 100$ μm have been extensively used in the past, a fourth combination of sensors using the CPI for $D < 100$ μm and the CIP for $D \geq 100$ μm is also used and is referred to as CPI + CIP in the following. This combination presumably helps mitigate the uncertainties with CIP measurements for $D < 100$ μm and minimize the impact of the statistical sampling problems for large crystals caused by the CPI sample volume.

Following McFarquhar et al. (2007b), the uncertainties in the CSI IWCs are estimated as ±15%. Twohy et al. (2003) showed that a different version of the CSI, the counterflow virtual impactor (CVI), could underestimate the total water content for mean volume diameters smaller than 30 μm; however, this is likely not an issue for TWP-ICE where the mean volume diameters are typically higher. On the other hand, a pressure-dependent sensor zero offset (or rolloff) for IWC occurred because of a delayed flow at lower pressure that meant IWCs gradually decreased outside of cloud. This is especially problematic in clear skies for IWC < 0.002 g m^{-3}. Therefore, only IWCs larger than this value are used and hereinafter the IWC measured by the CSI is assumed to be a reference IWC. In what follows the agreement will be denoted loosely as "good" when the difference between the IWCs calculated from the particle size distributions and the CSI is less than the expected uncertainty of the CSI measurements (15%).

3. The TWP-ICE case studies and data quality

To estimate the bulk microphysical properties of tropical ice clouds, data from the CPI, CDP, and CIP were needed. There are only three *Proteus* flights for which all these data are available during TWP-ICE: 27 January 2006, 29 January 2006, and 2 February 2006 (hereinafter called the 27/01, 29/01, and 02/02 flights). All these flights were performed during a so-called suppressed monsoon period that occurred immediately after a long period of intense monsoonal convection that ended around 24 January (May et al. 2008).

The 27/01 flight was performed from 0520 to 0930 UTC in bands of cirrus associated with a deep low pressure system over the Northern Territory (McFarquhar et al. 2007a). The flight altitude was between 14 and 16 km. These bands are also observed by the cloud radar and lidar at the Darwin ARM site from 25 to 29 January 2006 (not shown). Figure 1a shows the averaged size and habit distributions measured by the CPI, where the habits are classified using the technique of Um and McFarquhar (2009), which uses the following 11 habits: small, medium, and large quasi spheres (SQS, MQS, and LQS), columns (COL), plates (PLT), bullet rosettes (BR), aggregates of columns (AC), aggregates of plates (AP), aggregates of bullet rosettes (ABR), capped columns (CC), and unclassified particles (UCL). It must be noted that this figure provides an overall characterization of the ice particle habits generated during each flight but no indication about the temporal evolution of the dominant particle habit. As a result, this figure should not be interpreted in terms of microphysical growth processes by relating habits found in different diameter ranges, because different particle habits can be encountered at different times during the flights. To characterize this temporal evolution, Table 1 gives the dominant particle types for selected time intervals of the three flights.

Figure 1a shows that almost all particles with $D <$ 50 μm are classified as quasi spheres, with average $N(D)$ of almost 1 L^{-1} μm^{-1} peaking at 15 μm. This may in part be due to the resolution of the CPI, which is not high enough to distinguish complex shapes of these small ice crystals when particles are slightly out of focus (e.g., Ulanowski et al. 2004). In the 50–100-μm range, the fraction of non-quasi-spherical particles increases to around 50%. For particles with $D \sim 100$ μm, 50% were unclassified, and the other half was mostly bullet rosettes with a few plates and aggregates of plates. In the 100–300-μm range, the amount of UCL particles is quite large (around 40%), and the remaining fraction is essentially made of BRs, APs, and ACs with very small numbers of columns and plates also found. For particles with $D > 300$ μm, the fraction of unclassified particles is much smaller, and the dominant particles are BRs and ABRs, with small amounts of ACs. Particle habit classifications for different time intervals (given in Table 1) show that there are periods with more bullet rosettes

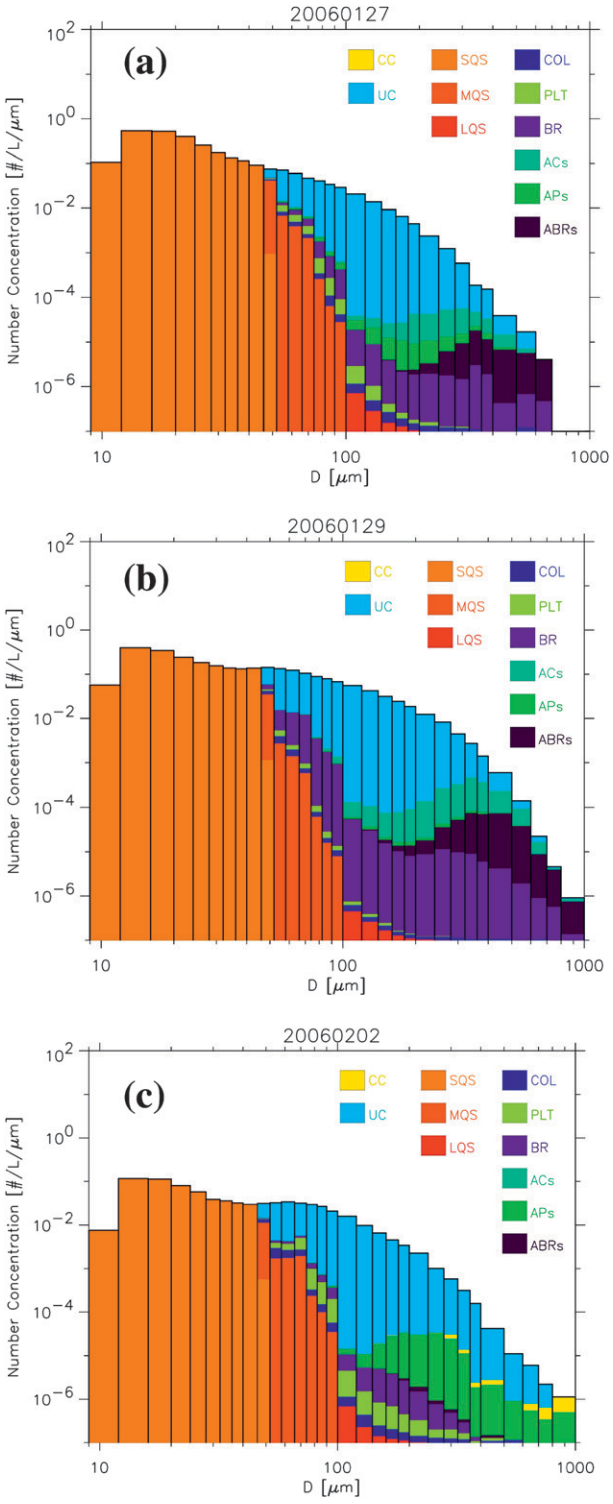

FIG. 1. The mean particle size distribution and particle habit classification derived from the CPI observations for the (a) 27/01, (b) 29/01, and (c) 02/02 TWP-ICE flights. The particle habit classification includes 11 habits detailed in the text. In the figure, the fraction of each habit is given for each D bin. Reproduction from Um and McFarquhar (2009).

and other periods with more plates, suggesting different environmental conditions or different growth histories of ice crystals across the different cirrus bands during the 27/01 flight. In terms of instrument performance, all sensors worked well from 0800 to 0930 UTC, but the CAS and CIP probes were not recording data for the first part of the flight. On the other hand, the CPI distributions as well as the CSI measurements can be used for the first part of the flight.

The 29/01 flight from 0550 to 0910 UTC was also conducted in aged cirrus bands. The flight altitude was between 12 and 15 km. The average CPI particle classification for this day (Fig. 1b) exhibits a pattern similar to that seen on 27/01. An important difference is that much smaller numbers of pristine plate crystals were found in the 29/01 cirrus layer in comparison with the 27/01 flight (8%–12% in the 100–300-μm range; Fig. 1a). An inspection of the particle classification as a function of time (not shown) indicates a smaller variability in the distribution of particle habits with time on 29/01 relative to that on 27/01, as also indicated in Table 1. The main observed change with time is a substantial increase in fraction of quasi-spherical particles, from 5% to 10% between 0545 and 0820 UTC to 60%–70% between 0820 and 0910 UTC. During the first part of the flight (before 0800 UTC) the CIP measurements are questionable (as will be shown later), and therefore only the CPI distributions were used for this flight portion.

The 02/02 flight was performed in a fresh deep anvil produced by deep convection that was forming over the Tiwi Island at the takeoff time of the *Proteus* (McFarquhar et al. 2007a). The flight altitude was between 12 and 15 km. The CPI particle classification in Fig. 1c is markedly different from the two other flights. The distribution of quasi-spherical particles is very similar in shape to the two other flights, but characterized by much smaller numbers (by a factor of 5–10 for $10 < D < 60$ μm), possibly owing to the progressive drying of the upper troposphere during this suppressed monsoon period (May et al. 2008). A drier troposphere will indeed preferably favor sublimation of the small ice crystals rather than production of small spherical ice particles from the deposition of water vapor. For $50 < D < 100$ μm, columns and plates dominate the nonspherical habits, while bullet rosettes dominated for the two other flights, especially on 29/01 (see Fig. 1b). For $D > 100$ μm, the difference with the two other flights is even more obvious, with a predominance of plates and aggregates of plates for the 02/02 flight, while BRs, ABRs, and ACs dominated for the 27/01 and 29/01 flights. On 02/02, all sensors worked well. Because this flight is characterized by rapid changes in dominant habits (see Table 1) and because the *Proteus* was frequently going

TABLE 1. List of the flight portions used in this study, the most representative particle habits found for small ($S < 100$ μm) and large ($L > 100$ μm) ice crystals (see text for particle type codes), and the most trusted combination or combinations of sensors for each flight portion. The dominant particle type is given first, and some others are given when in significant amounts. Combinations 1, 2, and 3 are the CDP + CIP, CPI, and CPI + CIP, respectively. If "132" is given as a most trusted combination, it means that CDP + CIP is most trusted, then CPI + CIP, then CPI. See text for more details.

Time period (UTC)	Most representative particle types ($S < 100$ μm, $L > 100$ μm)	Trusted sensor combination(s)
27/01 0700–0730	*S*: QS + BR + COL *L*: BR + ABR + AC	2
27/01 0812–0836	*S*: QS + PLT + COL *L*: PLT + AP+ AC + BR	132
27/01 0836–0851	*S*: QS + PLT *L*: none	2
27/01 0900–0918	*S*: QS + PLT *L*: AP + AC + PLT	132
27/01 0918–0936	*S*: QS + BR + COL + PLT *L*: BR + AC + ABR	132
29/01 0545–0612	*S*: QS + PLT *L*: BR + ABR + AC + AP	2
29/01 0640–0712	*S*: QS + COL *L*: BR + ABR + AC	2
29/01 0712–0758	*S*: QS + COL *L*: BR + ABR + AC	2
29/01 0803–0836	*S*: QS + BR *L*: BR + ABR + AC	213
29/01 0836–0900	*S*: QS + BR *L*: BR + ABR + AC	213
02/02 0210–0236	*S*: QS + COL *L*: BR	123
02/02 0258–0315	*S*: QS + COL + PLT *L*: AP + PLT + COL + CC	1
02/02 0328–0335	*S*: QS + COL + PLT *L*: AP + PLT + COL	1
02/02 0352–0400	*S*: QS + COL + PLT *L*: AP + PLT + COL	132
02/02 0400–0415	*S*: QS + COL *L*: AP + PLT + COL + CC	132
02/02 0430–0442	*S*: QS + PLT *L*: UCL + AP + PLT + COL	132
02/02 0445–0502	*S*: QS *L*: very few QS + BR + ABR	132
02/02 0508–0530	*S*: QS *L*: very few QS + BR + ABR	132

in and out of cloud, small segments of flights were processed separately from each other.

4. Comparison of the in situ microphysical sensors deployed during TWP-ICE

In this section, the impact of shattering of large ice crystals on the tips of probes used during TWP-ICE is examined. Then the overlap of the range in D of the different probes is used to compare probe measurements, to provide an estimate of the scaling factor needed to determine the CPI size distributions, and to develop semiobjective elements for interpreting differences between IWC derived from size distributions and IWC directly measured by the CSI. In this analysis, let us recall that two reference measurements are considered in order to estimate the CPI scaling factor and to evaluate the different size distribution measurements from the TWP-ICE probe combinations: the size distributions measured by the CIP for $D \geq 100$ μm, and the IWCs measured by the CSI.

a. Impact of shattering on the TWP-ICE in situ microphysical measurements

As discussed in section 2, all probes used during TWP-ICE can potentially produce some shattering of large ice crystals. For some of them, though, the magnitude of this contamination has not been documented so far. Regarding the CPI probe, particle shattering would typically produce more than one particle per CPI frame (associated with very short interarrival times), and the occurrence of multiple particles per frame should increase with the CIP concentration of large particles. Using all data from the three TWP-ICE flights described previously, it is found that among 180 905 particles imaged by the CPI, 178 102 (98.45%) particles were 1 particle per frame, while 2596 (1.43%), 186 (0.10%), 16 (0.01%), and 5 (0.003%) were 2, 3, 4, and 5 particles per frame, respectively. Similar numbers are obtained for each flight separately. These occurrences of multiple particles per frame are small, indicating that shattering of ice particles by the CPI during TWP-ICE was apparently not significant. The number of ice particles per frame has also been studied as a function of the concentration of particles with $D > 300$ μm as measured by the CIP probe (other thresholds from 150 to 300 have been used, producing little change). This is reported in Fig. 2d. From this figure there is no indication of an increase of the occurrence of multiple particles per frame for increasing concentrations of large particles by the CIP, suggesting a minimal impact of shattering in these CPI data.

Some studies also recently showed that the number of fragments produced by shattering should increase with mass (e.g., Heymsfield 2007; McFarquhar et al. 2007a; Jensen et al. 2009). The IWC as measured by the CSI during TWP-ICE has therefore been displayed as a function of the total concentration $N_{9\text{–}50\mu\text{m}}$ obtained by integrating the CPI, CDP, and CAS distributions from 9 to 50 μm. This range was chosen because it is the common range of the CDP, CPI, and CAS probes. Figure 2a shows the result of this analysis using the data from the CPI probe. From this figure a small correlation is

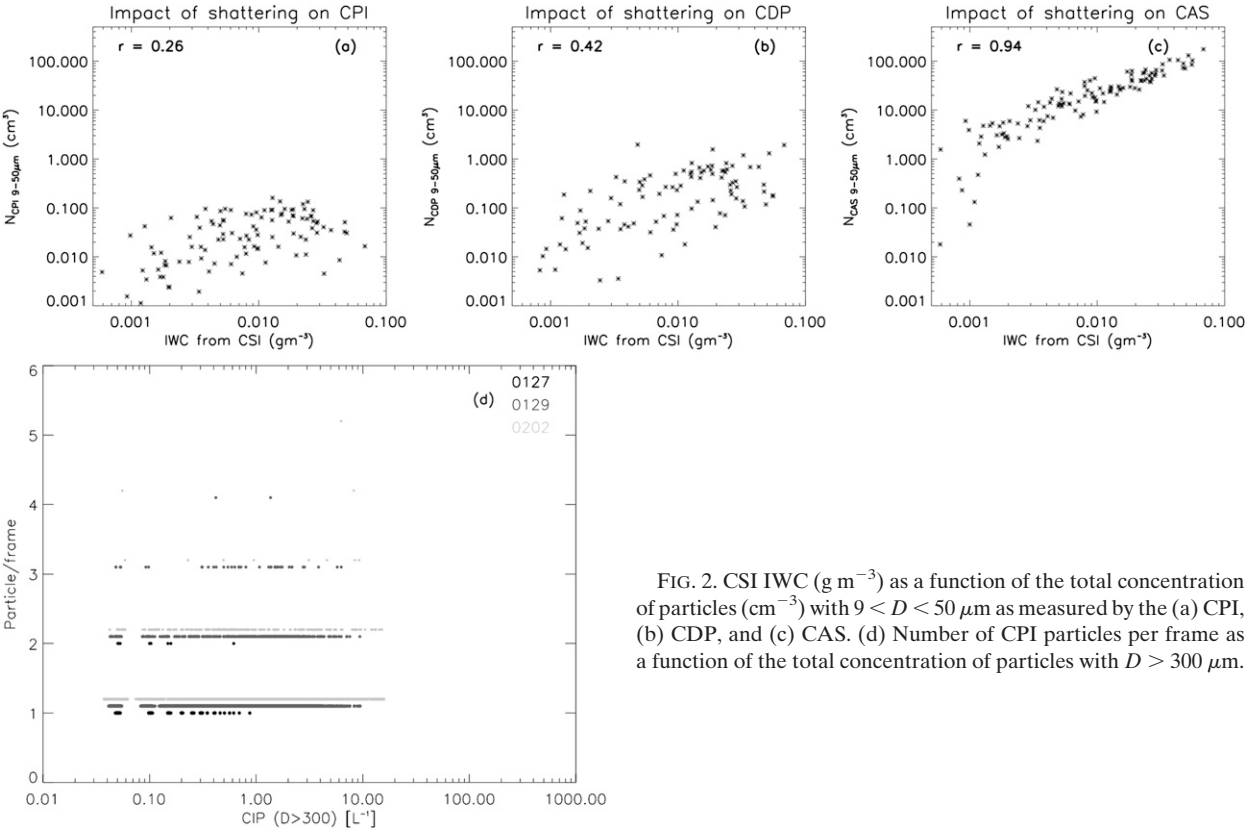

FIG. 2. CSI IWC (g m^{-3}) as a function of the total concentration of particles (cm^{-3}) with $9 < D < 50$ μm as measured by the (a) CPI, (b) CDP, and (c) CAS. (d) Number of CPI particles per frame as a function of the total concentration of particles with $D > 300$ μm.

observed (correlation coefficient of 0.26), which is in the same range as the values obtained in Jensen et al. (2009) using the 2-Dimensional Stereo (2D-S) probe (Lawson et al. 2006) with particle shattering removed in aged tropical anvils during the Tropical Composition, Cloud, and Climate Coupling (TC4) campaign in Costa Rica. The scatter also appears to be fairly similar to the TC4 observations. This moderate correlation is therefore likely due to the microphysical growth processes and not predominantly due to shattering, although a contribution from shattering cannot be excluded. Because the TWP-ICE observations have been collected at relatively high altitudes (from 12 to 16 km) as compared with TC4 (9–12 km), the contribution of small natural ice crystals to the bulk microphysical properties at such high altitudes in cirrus clouds may be more significant. This point will be studied further in section 6c. In any case, it produces a much lower correlation than what has been reported for shattering in the literature. These results therefore suggest that the CPI observations during TWP-ICE are not contaminated significantly by shattering.

The same analysis has been conducted for the CDP (Fig. 2b) and the CAS (Fig. 2c) probes. The correlation between $N_{9-50\mu m}$ and IWC is somewhat larger for the CDP (correlation of 0.42). However, it is still in the range reported by Jensen et al. (2009) for the 2D-S. Also the total concentrations derived from the CDP in this range are systematically larger than those derived from the CPI. This increase in correlation and $N_{9-50\mu m}$ suggests that shattering of large crystals on the CDP probe tips is probably larger than that of the CPI. It is to be noted that the fact that this correlation is still in the range of correlations obtained using the 2D-S with shattered particles removed in TC4 could be an indication of some other unidentified problems with the CDP measurements (see also results from section 4d). However, the magnitude of this contamination will remain unknown for TWP-ICE, as particle interarrival times have not been measured during TWP-ICE, as discussed in section 2, preventing any correction of these data. From Fig. 2 it appears, however, that this contamination is in any case much smaller than for the CAS.

As expected from earlier analyses of the TWP-ICE dataset (McFarquhar et al. 2007a), the total concentrations of small ice crystals as measured by the CAS (Fig. 2c) are systematically much higher than the CDP and CPI total concentrations (Figs. 2a,b). The correlation with the IWC measured by the CSI is also very high (0.94, see Fig. 2c), which is consistent with the findings of Jensen et al. (2009). These CAS total concentrations

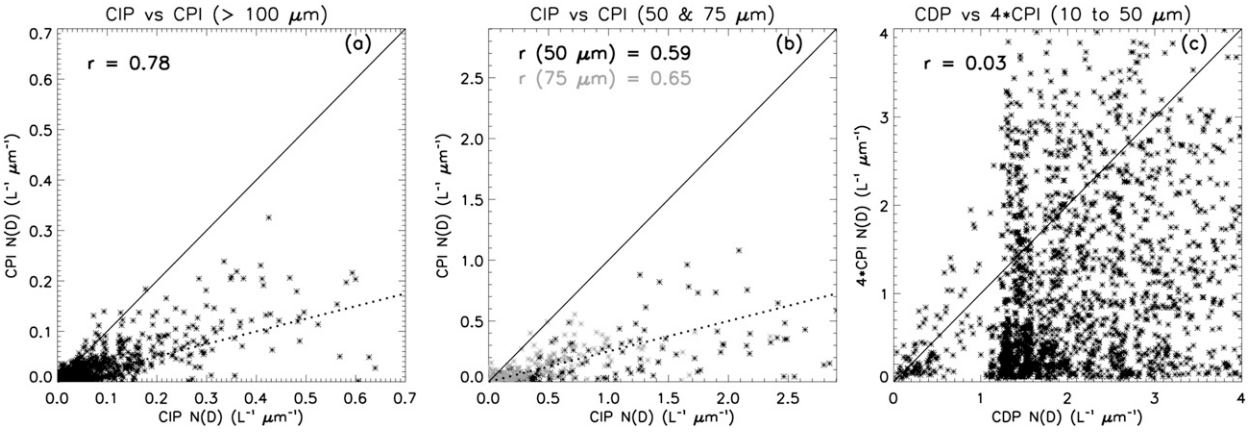

FIG. 3. Comparison of the different sensors in their overlapping D ranges using all TWP-ICE flights: (a) the CIP and CPI $N(D)$ for D bins larger than 100 μm, (b) the CIP and CPI $N(D)$ in the 50- (black) and 75-μm (gray) bins, and (c) the CDP $N(D)$ and the CPI $N(D)$ multiplied by 4 for bins in the 10–50-μm range. The 1:1 (solid) and 0.25:1 (dotted) lines are displayed in (a) and (b). The correlation between the measured $N(D)$ is also given in all panels.

of small ice crystals are a factor of 7–30 larger than the CDP and a factor of 9–40 larger than the CPI, depending on the flight segment. In an attempt to mitigate the shattering problem in TC4 CAS observations, the CAS probe was mounted without the protruding shroud used during TWP-ICE, thereby offering fewer surfaces for potential shattering of large crystals. When comparing TC4 results in Jensen et al. (2009, their Fig. 5a) and our TWP-ICE results (Fig. 2c), it seems that this choice was wise, because the total concentrations (which are assumed to be artificially generated by shattering) for any given IWC are lower by a factor of 10 or so in TC4 than in TWP-ICE.

It must be noted that the conclusions drawn in this section should not be used to make the same statement for other campaigns. Indeed, the way the probes are mounted can be crucial [see comparisons between two 2D-S probes in Jensen et al. (2009)] and the concentration of large crystals may well be very different from what was encountered during TWP-ICE, producing therefore more or less contamination by shattering.

b. Estimate of the unknown CPI scaling factor

To estimate the unknown scaling factor of the CPI, the CIP measurements for bins with $D \geq 100$ μm are taken as a reference (see discussion in section 2). Figure 3a shows this comparison between CPI and CIP with all TWP-ICE flights combined (the CPI and CIP probes worked well together in four flights). First it is noted that the correlation of those two measurements is high (0.78), which is also the case when each flight is considered separately (correlation ranging from 0.7 to 0.85, not shown). As also clearly seen in Fig. 3a, there is a systematic underestimation of $N(D)$ by the CPI when compared with the CIP measurements, which is assumed in this study to be the result of the unknown scaling factor of the CPI measurements, as discussed in section 2. The (CPI/CIP) $N(D)$ ratio is found to be 0.26 when data from all TWP-ICE flights are combined. This result suggests that the CPI $N(D)$ are underestimated by a factor of approximately 4. Figure 4 illustrates on a flight segment the effect of scaling these CPI size distributions, by displaying the combined CPI + CIP distributions before and after applying the scaling factor of 4 to the CPI $N(D)$. From this figure it appears clearly that the CPI and CIP size distributions are much more continuous for $50 < D < 200$ μm after the scaling. In the remainder of this paper the CPI $N(D)$ are thus multiplied by a factor of 4. Slightly anticipating the results of comparisons with the CSI IWCs, it will be shown that

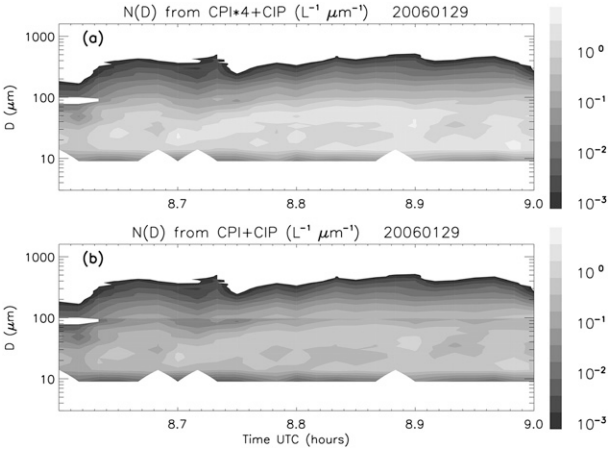

FIG. 4. Measurements of $N(D)$ by the CPI + CIP combination (a) when the CPI $N(D)$ is multiplied by a factor of 4 and (b) when it is not for the 29/01 flight from 0821 to 0900 UTC.

the use of this objective estimate of the CPI scaling factor produces IWCs that are statistically consistent with the CSI IWCs (i.e., within the accuracy of the CSI measurements).

c. *Assessment of the CIP measurements in the 50–75-μm range during TWP-ICE*

As discussed in section 2, the measurements of the CIP probes in the 50–75-μm range are expected to contain large errors, although they must be used to avoid a gap in the size distributions derived from the CDP + CIP combination. These measurements are assessed using the CPI measurements in this same range. The result of these comparisons using all TWP-ICE flights is shown in Fig. 3b. First, the correlation of the two measurements for the 50- and 75-μm bins of the CIP is still relatively high (0.6 and 0.65, respectively), although not as high as with the CIP measurements for $D \geq 100$ μm (0.78). This probably indicates that although these measurements are less accurate, they are not predominantly generated artificially by the measurement uncertainties of the CIP in that 50–75-μm range (discussed in section 2). Also an estimate of the CPI/CIP ratio for these two diameter bins is 0.25, which is quite consistent with the findings of section 4b, giving additional confidence that these measurements can be used (at least those collected during the TWP-ICE experiment). In the remainder of this paper the CIP in the 50- and 75-μm bins are therefore used in the CDP + CIP combination.

d. *Assessment of the CDP measurements during TWP-ICE*

As discussed in section 2, the CDP probe is relatively new and its performance still needs to be fully assessed. Because the unknown CPI scaling factor has been estimated in the previous subsection, the scaled CPI distributions and the CDP distributions can now be compared for bins with $9 \leq D \leq 50$ μm for purposes of qualitative assessment of the CDP measurements during TWP-ICE. This comparison is given in Fig. 3c. The scatter is clearly very large, and the correlation calculation indicates that there is no correlation between these two small particle concentration measurements. These differences can be either due to the sampling problem of the CPI probe (see discussion in section 2) or to an unidentified problem with the CDP. It is to be noted that the TWP-ICE dataset does not allow any further statement to be made about which probe is right (and they may both be wrong) because we have no reference measurement in this diameter range. New datasets progressively becoming available, using in particular the 2D-S probe (Lawson et al. 2006) and probes with tips designed to minimize the impact of particle shattering, will certainly help shed more light on the accuracy of the small ice particle concentration measurements by the CPI and the CDP. Both CPI and CDP $N(D)$ measurements will be used in what follows, and the differences between the two measurements will be kept in mind and used when comparing the bulk cloud microphysical properties derived from all probe combinations in section 6.

5. "Best estimates" of density and projected area

It is common that calculations of bulk microphysical parameters from particle size distribution measurements be carried out using a single m–D (or ρ–D) relationship and a single A–D relationship (e.g., Delanoë et al. 2005). Several studies have used a relationship derived for ice aggregates in midlatitude clouds (Brown and Francis 1995) or more recently temperature-dependent relationships from a larger sample of midlatitude and tropical ice clouds (Heymsfield et al. 2007). On the other hand, McFarquhar et al. (2002) combined size and shape distributions derived from two-dimensional cloud imaging probe data with m–D relationships for different particle shapes to compute the bulk microphysical properties. However, more detailed ice crystal classifications, such as that presented in Um and McFarquhar (2009), are now available that should improve such computations of bulk microphysical properties. Here, the particle classification of Um and McFarquhar (2009) for the 27/01, 29/01, and 02/02 flights (see Fig. 1) in each D bin is used to derive "best estimates" of the density and particle projected area in each D bin, which will be denoted as $\overline{\rho(D)}$ and $\overline{A(D)}$ in the following. The principle here is to use the fraction of each particle habit derived by the CPI classification at the 60-s time resolution and individual ρ–D and A–D statistical relationships for each habit.

As discussed previously, the original CPI classification has 11 classes. From these, four ρ–D and five A–D relationships were used for our calculations. The smaller number of classes is due to the fact that some particle habits are characterized by the same ρ–D or same A–D relationships in the literature. The details of these classes are given in the appendix. The treatment of the UCL class is problematic since, as shown in Fig. 1, this class can occasionally represent 30%–40% of the total number of particles. In the following, we have used the ρ–D and A–D relationships of Brown and Francis (1995) (see the appendix), because visual inspection of the unclassified particles indicated that most of them were aggregates. Sensitivity tests have also been conducted, by using the most frequent and second most frequent particle habit. These sensitivity tests (not shown) clearly indicate that the use of the Brown and Francis (1995) aggregates habit produces the best agreement with the

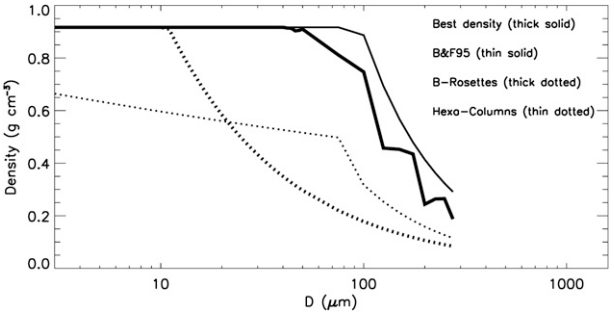

FIG. 5. Ice particle density as a function of maximum diameter D for the 27/01 flight averaged over the 0821–0836 UTC time period using different ρ–D relationships: (a) the best estimate of density proposed in this study (thick solid line), (b) the Brown and Francis (1995) aggregates (thin solid line), (c) the Mitchell (1996) bullet rosettes (thick dotted line), and (d) the Mitchell (1996) hexagonal columns (thin dotted line).

CSI IWCs, while the use of the most or secondmost frequent habit in the classification systematically tends to slightly degrade the agreement with the CSI, by a small amount though in most cases (less than 5%–10% on IWC). For the situation when there is intermittently no CPI data, the closest particle habit classification available in time was used.

Finally, the best estimates $\overline{\rho(D)}$ and $\overline{A(D)}$ are obtained using

$$\overline{\rho(D)} = \sum_{i=1}^{4} \text{habit\_fraction}(i) \times \rho_i(D) \quad \text{and} \qquad (1)$$

$$\overline{A(D)} = \sum_{i=1}^{5} \text{habit\_fraction}(i) \times A_i(D), \qquad (2)$$

where $\rho_i(D)$ and $A_i(D)$ are the ρ–D and A–D relationship for habit category i. This technique will be referred to as Best Estimate of Area and Density (BEAD) in the following.

In Figs. 5 and 6, the impact of using $\overline{\rho(D)}$ is shown. The same impact is not shown for the projected areas, because the differences found are similar to what will be discussed for the densities, and because there is no reference for evaluation. Figure 5 shows the different $\overline{\rho(D)}$ used for the calculations carried out to get the IWC time series of Fig. 6: aggregates using the Brown and Francis (1995) relationship, bullet rosettes (thick dotted line), and hexagonal columns from Mitchell (1996; thin dotted line). This shows that the $\overline{\rho(D)}$ of the models for both the small and large ice crystals can differ by up to a factor of 2 in some D ranges (e.g., the differences between ρ in the 10–100-μm range between columns and aggregates). When using the particle habit fractions and the $N(D)$

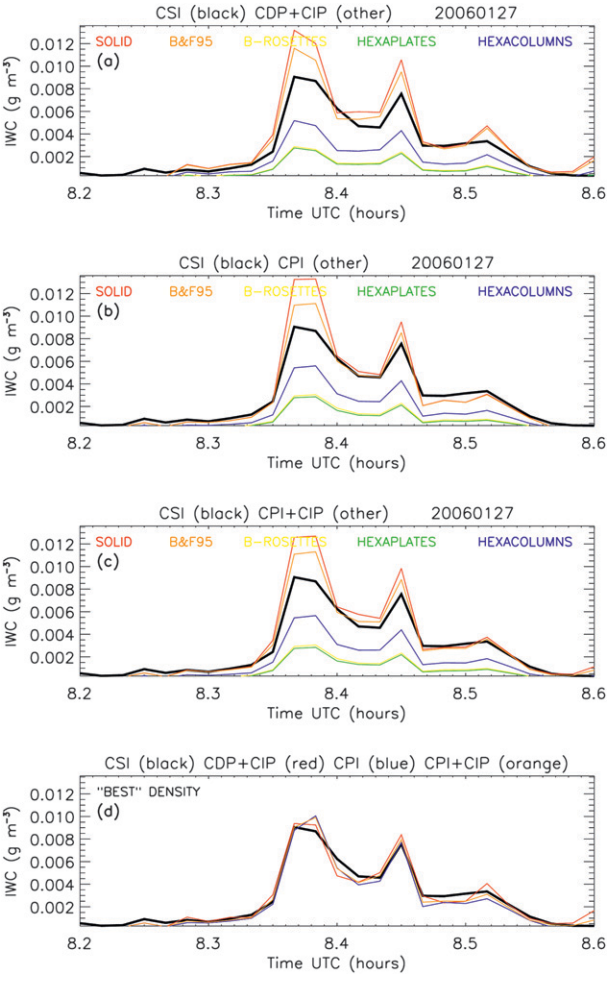

FIG. 6. Time series of IWC derived from the CSI (black), different combination of sensors, and with different assumptions on the ρ–D relationships: solid spheres (red), aggregates (orange), bullet rosettes (yellow), hexagonal plates (green), and hexagonal columns (blue). (a) CSI vs CDP + CIP, (b) CSI vs CPI, and (c) CSI vs CPI + CIP. (d) The same comparison when the best estimate of density is used for each combination: CDP + CIP (red), CPI (blue), and CPI + CIP (orange). Note that the CPI $N(D)$ have been multiplied by 4.

measurements in Eq. (1), the $\overline{\rho(D)}$ denoted as best estimate in Fig. 5 is obtained. The retrieved $\overline{\rho(D)}$ is found similar to the density produced with the Brown and Francis (1995) aggregates with, however, smaller $\overline{\rho(D)}$ for the largest D, which is in good agreement with the density produced when assuming bullet rosettes and aggregates of columns.

To characterize the impact of having different measurements of $N(D)$ from the different sensor combinations, the $N(D)$ from the CDP + CIP, CPI and CPI + CIP combinations were used to calculate IWC using the "pristine" densities (see the appendix) and $\overline{\rho(D)}$ derived from Eq. (1). Figures 6a–c show the results for the

pristine densities using each combination of size distributions. Figure 6d shows the results for the three combinations but using $\overline{\rho(D)}$.

From the first three panels, it is seen that the IWC estimated from different density assumptions can vary by up to a factor of 5 for the peaks. For this particular flight portion, the best match with the CSI IWC is obtained when assuming the aggregates habit for all three sensor combinations, but with a general overestimate of 10%–20% of the CSI IWC. When $\overline{\rho(D)}$ is used (Fig. 6d), the derived IWCs agree within 5% with the CSI IWC. Section 6 shows that this result also holds statistically when considering the whole TWP-ICE dataset, with errors on IWC reduced using $\overline{\rho(D)}$ when compared with calculations using a single particle habit. From Table 1, it appears that on some occasions the dominant particle type can change rapidly (e.g., a switch from large bullet rosettes and aggregates of bullet rosettes to plates and aggregates of plates is observed for the 27/01 flight). These rapid changes are taken into account in the present approach, while it can be the source of major uncertainty when assuming a single ρ–D for a whole flight. The TWP-ICE analysis shows that this 60-s update of $\overline{\rho(D)}$ is crucial for improved estimates of IWC. This BEAD technique will also be compared in section 6 with the well-established WLAP technique for deriving IWC from the CPI measurements (Baker and Lawson 2006).

6. Impact of the differences in size distributions on bulk microphysical properties

In section 4, different approaches for deriving the particle size distributions were developed and compared. In section 5, the BEAD technique was developed to determine the statistical relationships between crystal density, projected area, and maximum crystal dimension needed to derive the bulk microphysical properties. In this section particle size distributions at 60-s resolution measured by the CAS + CIP, CDP + CIP, CPI and CPI + CIP for selected flight times (as explained in section 2) in both aged cirrus clouds and the fresh anvil are used to derive the bulk microphysical properties and the associated uncertainties. The impact of the differences in size distributions is first analyzed in detail from each time series of TWP-ICE, and then quantified statistically using all TWP-ICE data available. The contribution of small ice crystals to the cloud microphysical properties of the TWP-ICE cirrus clouds is finally estimated and discussed.

Let us start with an illustration of the difference in size distributions measured by the four probe combinations during TWP-ICE. Figure 7 shows the mean particle size distributions measured on 27/01 from 0812 to 0836 UTC

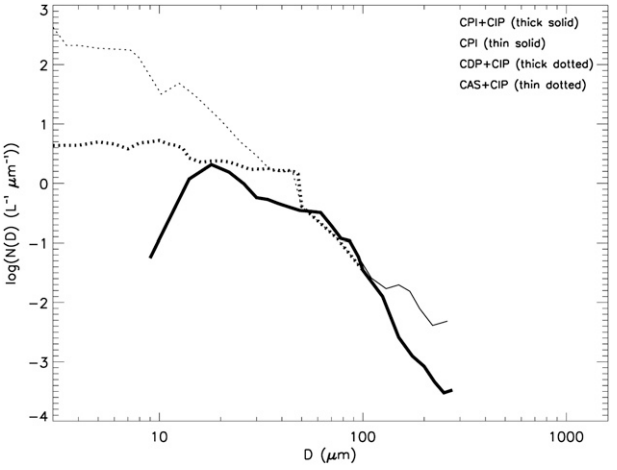

FIG. 7. Mean particle size distribution $N(D)$ measured by the following four combinations during the 27/01 flight between 0812 and 0836 UTC: (a) CDP + CIP (thick dotted line), (b) CAS + CIP (thin dotted line), (c) CPI +CIP (thick solid line), and (d) CPI alone (thin solid line). Note that the CPI $N(D)$ have been multiplied by 4.

(the same period as that shown in Figs. 5 and 6), when all sensors worked well and produced similar time series of IWC. This figure is fairly representative of the differences in size distributions observed during TWP-ICE. This figure is quite striking in that very large differences are found between the four probe combinations in some D ranges. Now the question we will address is how these differences between probe combinations translate into differences in the bulk microphysics parameters. For this purpose, the IWC, visible extinction [α, calculated as $\int N(D)A(D)\,dD$], total number concentration [N_T, calculated as $\int N(D)\,dD$], and effective radius [R_{EFF}, which is calculated in the present study as proportional to the ratio of IWC to extinction, following the definition of Stephens et al. (1990)] were calculated from each of the four estimates of the size distribution and the $\overline{\rho(D)}$ and $\overline{A(D)}$ produced using the BEAD technique. Table 1 gives a detailed description of the flight portions included in the analysis, the dominant small and large particle types, and the most trusted instrumental combinations for each time period, where the trusted combinations were identified as follows. Again, let us recall that the CSI IWC is assumed to be the reference. As reported in McFarquhar et al. (2007b), it is believed to be accurate to within 15%. To evaluate the different probe combinations, an upper bound for IWC was first calculated from each combination assuming that all particles were solid spheres of density 0.917 g cm^{-3}. IWC derived in this manner should largely overestimate the CSI IWC. If this upper bound for IWC was smaller than the CSI IWC, it was therefore assumed that at least

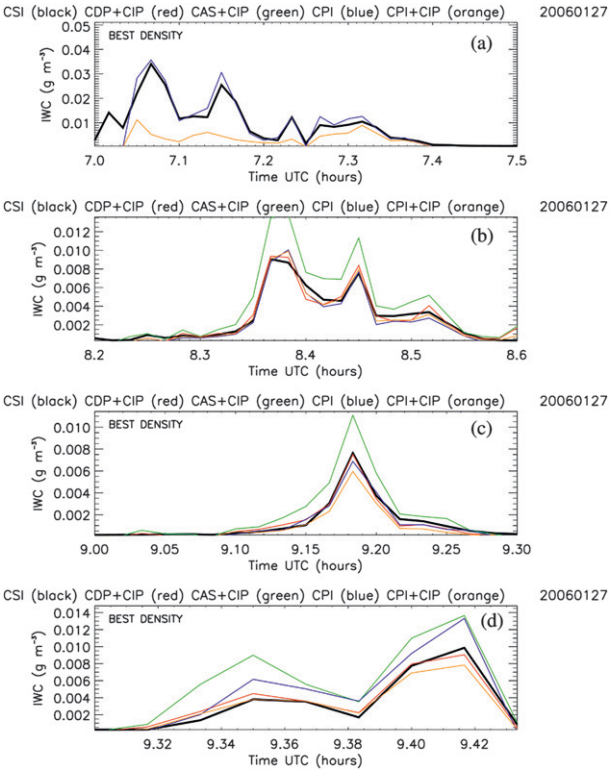

FIG. 8. Time series of IWC measured on 27/01 by the CSI (black), the CDP + CIP (red), the CPI + CIP (orange), and the CPI alone (blue) (a) from 0700 to 0730 UTC, (b) from 0812 to 0851 UTC, (c) from 0900 to 0918 UTC, and (d) from 0918 to 0926 UTC. The best estimate of density is used for these computations. Note that the CPI $N(D)$ have been multiplied by 4.

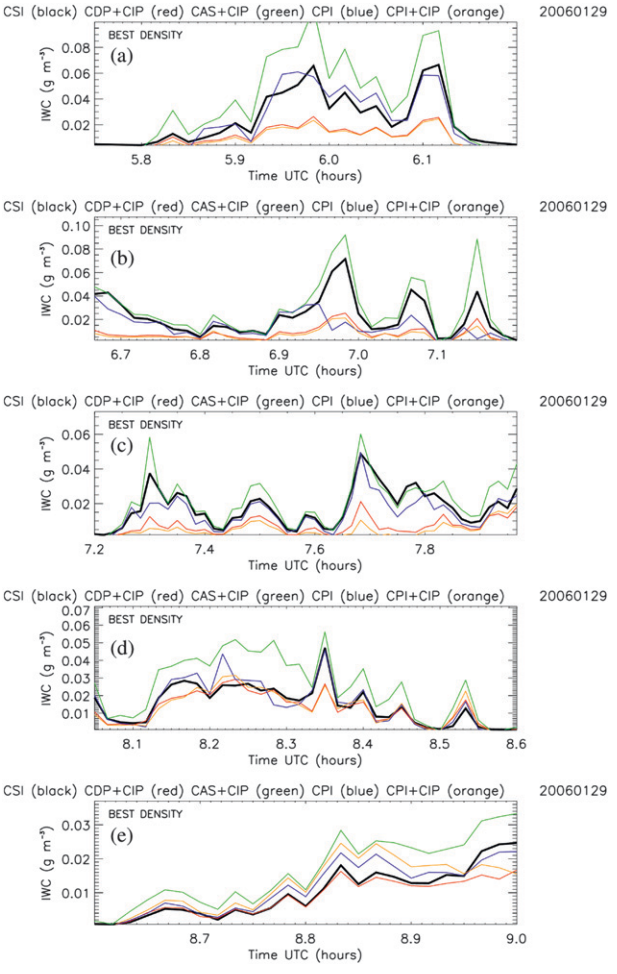

FIG. 9. As in Fig. 8, but for the 29/01 flight and (a) from 0545 to 0612 UTC, (b) from 0640 to 0712 UTC, (c) from 0712 to 0758 UTC, (d) from 0803 to 0836 UTC, and (e) from 0836 to 0900 UTC.

one of the probes in that sensor combination was not working properly, and the combination was not used. In addition, all flight portions for which the best estimate of IWC of a given sensor combination produced a discrepancy larger than a factor of 2 from the CSI IWC were discarded. The most trusted sensor combination for a given period was that which produced the best agreement with the CSI IWC. Individual particle size distributions from the discarded combinations were then carefully scrutinized. The majority of the time one of the sensors failed resulting in a large underestimation of IWC. For each flight portion, at least one sensor combination had to work properly to be included in the analysis.

a. Flight-by-flight analysis of the retrieved and measured IWC time series

Figures 8–10 show time series comparisons between the CSI IWCs and IWCs derived from the four probe combinations CAS + CIP, CDP + CIP, CPI and CPI + CIP and the best estimates of $\overline{\rho(D)}$ and $\overline{A(D)}$ for the 27/01, 29/01, and 02/02 flight, respectively. Statistics of the mean fractional differences between the IWC derived from each combination and the CSI IWCs are also reported in Table 2 for each flight portion in Figs. 8–10. For the 27/01 flight (Fig. 8), the CIP probe was working only intermittently, and thus for some flight portions only the CPI estimates are available (as reported in Table 1). For other periods the three combinations CDP + CIP, CPI, and CPI + CIP are available. The agreement with CSI for this flight is good for all time periods (Fig. 8), with mean fractional differences of less than 5% in absolute value (Table 2). It is interesting to note that this good agreement holds both for the small (down to 1–2 mg m^{-3}, Figs. 8b–d) and the larger (up to 40 mg m^{-3}, Fig. 8a) IWCs. The CAS + CIP combination produces a large positive bias (from 50% to 100% depending on the value of IWC).

For the 29/01 flight (Fig. 9), the CIP probe seems to have unreported and unidentified problems between 0545 and 0758 UTC, with artificially low $N(D)$

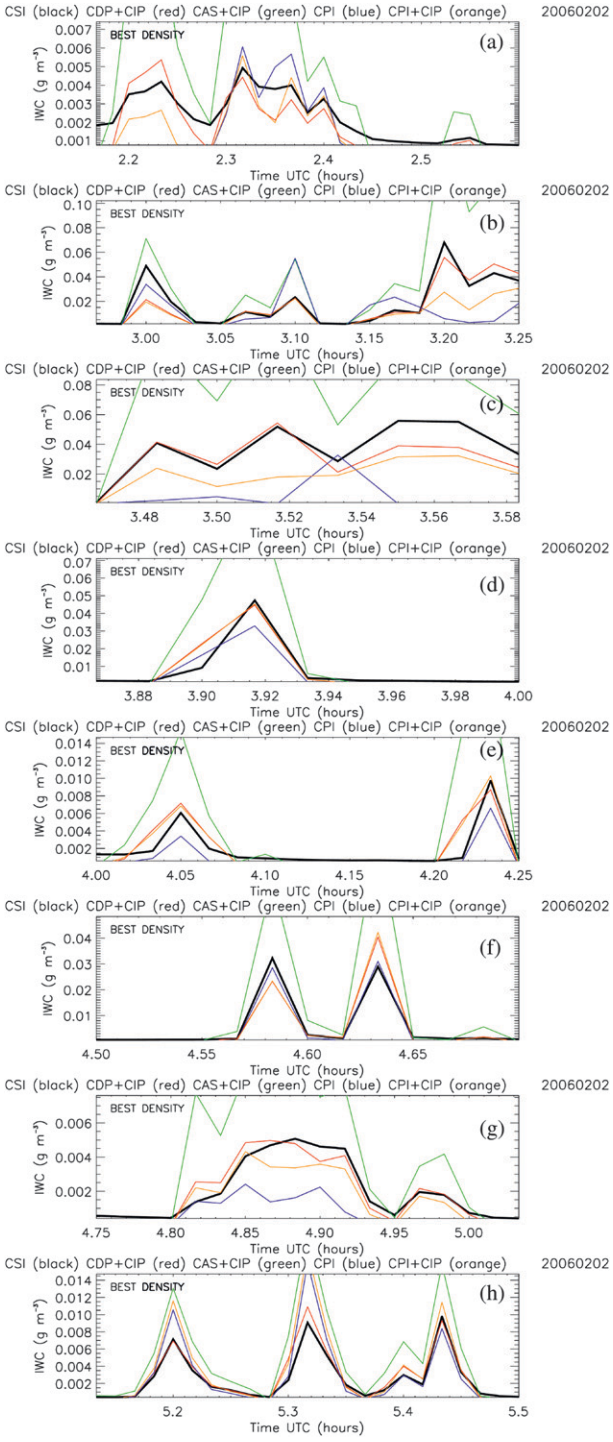

FIG. 10. As in Fig. 8, but for the 02/02 flight and (a) from 0210 to 0236 UTC, (b) from 0258 to 0315 UTC, (c) from 0328 to 0335 UTC, (d) from 0352 to 0400 UTC, (e) from 0400 to 0415 UTC, (f) from 0430 to 0442 UTC, (g) from 0445 to 0502 UTC, and (h) from 0508 to 0530 UTC.

TABLE 2. Mean IWC fractional difference between each sensor combination (CDP + CIP, CPI, and CPI + CIP) and the CSI IWCs for the different flight portions used to produce Figs. 8–10. Table cells are empty when the sensor combination was not working (see reports in Table 1) or when there were too few points in the calculations (less than 5).

Date and time period (UTC)	CDP + CIP mean fractional error (%)	CPI mean fractional error (%)	CPI + CIP mean fractional error (%)
27/01 0700–0730		9.3	
27/01 0812–0836	0.0	−11.6	−5.1
27/01 0900–0918	−3.7	−2.9	−21.6
27/01 0918–0926	3.3	39.5	−7.6
29/01 0545–0612		5.9	
29/01 0640–0712		−23.4	
29/01 0712–0758		−16.7	
29/01 0803–0836	−4.3	3.2	−3.8
29/01 0836–0900	−6.4	19.4	34.9
02/02 0210–0236	−4.5	12.0	−14.5
02/02 0258–0315	−2.3	12.4	−22.5
02/02 0328–0335	−13.6		−44.9
02/02 0400–0415	3.6	−82.5	9.2
02/02 0430–0442	−7.4	−5.9	−3.7
02/02 0445–0502	0.8	N/A	−15.9
02/02 0508–0530	21.3	18.9	47.2

corresponding to the large underestimates of IWCs seen in Figs. 9a–c. It is believed that the CIP did not work properly for this time period because IWC calculations assuming that all ice particles were spherical with a density of 0.917 g cm^{-3} led to IWCs smaller than the CSI IWCs. As a result, only the CPI combination was used for the 0545–0758 UTC time period. For the 0758–0900 UTC period, the three combinations were retained. For this latter period the CDP + CIP combination provides the best agreement with the CSI IWCs overall (around −5% mean fractional difference, see Table 2). For the first period the agreement between the CPI and CSI IWC is also good (Figs. 9a–c, corresponding to mean fractional differences ranging from −23 to +6%, Table 2), except from 0657 to 0712 UTC (Fig. 9b). For this time period (not shown) the CPI number concentrations for $30 < D < 50$ μm were much lower than those measured by the CDP, which would be the reason for this discrepancy. The reason for this behavior of the CPI is unknown. Interestingly, between 0640 and 0758 UTC on the 29/01 (Figs. 9b,c) the CAS + CIP combination produces a good agreement with the CSI IWCs. However, this apparent good agreement results from cancelling errors due to overestimated concentrations of small particles and artificially low concentrations measured by the CIP for this period. For the second time period, large overestimations of IWCs of the same order of magnitude as those found for the 27/01 flight are found for the CAS + CIP combination (Figs. 9d,e).

For the 02/02 flight, the most trusted combination was the CDP + CIP combination (fractional differences from CSI ranging from −14 to +21%, see Table 2), but the CPI and CPI + CIP combinations also produced reasonable agreement for a large portion of the flight (mean fractional differences from CSI ranging from −82% to +19% for the CPI, and from −45 to +47% for the CPI + CIP, Table 2). Figure 10 shows that there are also intermittent times for which fractional differences are much larger than the expected uncertainties of the CSI (e.g., at 0300 UTC, Fig. 10b). The reason for these larger differences has not been identified, since a closer inspection of the individual distributions did not reveal any obvious problem in the distributions. The overestimations of IWC produced by the CAS + CIP combination are particularly large for this flight, and can reach up to a factor of 3 (Fig. 10).

In some instances in Figs. 8–10, the CPI + CIP combination produces smaller IWCs than when only the CPI is used. This is in apparent contradiction with the expected statistical sampling problems for large crystals caused by the CPI sample volume, which would tend to produce the opposite. A detailed inspection of the individual distributions in these cases indicates that these larger IWCs calculated with the CPI alone occur when the CPI measures larger concentrations than CIP in the 100–300-μm diameter range (not shown). The reason for this is unknown at this stage.

b. *Statistical error analysis of the retrieved TWP-ICE bulk microphysical properties*

To produce a quantitative estimate on the accuracy of the bulk properties, an error analysis for IWC and an impact analysis for the other bulk microphysical properties were carried out. The error analysis on IWC consists of a mean and standard deviation of the fractional difference between each combination and the CSI IWC, both for all IWCs and per IWC bin. This analysis includes the results from all three TWP-ICE flights. Because most IWCs measured during TWP-ICE were less than 0.02 g m^{-3}, two error analyses were carried out with two bin resolutions: bin resolution of 0.001 g m^{-3} including only data with IWC $<$ 0.02 g m^{-3}, and bin resolution of 0.005 g m^{-3} including all IWCs. A minimum threshold of 2.0×10^{-3} g m^{-3} was also considered to avoid times when the CSI was most likely affected by the pressure-dependent zero offset (rolloff) problem discussed in section 2. The result of this IWC error analysis is given in Fig. 11a for the small IWCs, and in Fig. 11b for all IWCs with a larger bin resolution. When all IWCs are considered (Fig. 11b), the mean fractional errors are very small for the CPI + CIP (2.2%), CPI (−0.8%), and CDP + CIP (−1.1%) combinations, with standard deviations of 7%–9%. All combinations therefore seem to provide good estimates of IWC despite the large variability and uncertainty in the size distributions. It is interesting to note that these errors are smaller than the errors in IWC measurements of the CSI (15%; McFarquhar et al. 2007b). It is also noteworthy that the CPI and CPI + CIP combinations produce increasingly larger uncertainties for larger IWCs (Fig. 11b), which can reach a 30%–40% underestimation for the CDP + CIP combination for IWCs of 0.045 g m^{-3}. In contrast, and as expected from earlier studies (e.g., McFarquhar et al. 2007a; Heymsfield 2007), the CAS + CIP combination produces a large mean fractional error of 95%, with a standard deviation of 17%, much larger than the expected error of the CSI measurements.

For the small IWCs (Fig. 11a), the same conclusions as those obtained for all IWCs were reached, with relatively small mean fractional errors in derived IWC (less than 2% for the CDP + CIP and CPI combinations, 6.6% for the CPI + CIP combination), and only slightly larger standard deviations of the fractional difference, ranging from 8% to 12%. This error magnitude is compatible with the accuracies needed for the assessment of ground-based radar–lidar retrievals. The CDP + CIP combination and the CPI appear to produce the best agreement with the CSI IWC of the four combinations (see Figs. 11a,b). This result seems to indicate that the fact that small concentrations of ice particles (less than 1.5 L^{-1} μm^{-1}) that are below the threshold of the CDP do not impact the statistical estimate of IWC. The good agreement produced by the combinations including the CPI for the IWC comparisons also independently validates the scaling factor of the CPI concentrations, which was estimated in section 4.

The BEAD technique proposed in section 5 to minimize errors due to the ρ–D and A–D relationships can be compared with other techniques. A well-established method is the so-called width, length, area, and perimeter (WLAP) technique (Baker and Lawson 2006) that uses the CPI image width, length, area, and perimeter to compute IWC without having to classify the CPI images by habit. This is a much more efficient method than the BEAD technique in this respect. It is therefore very interesting to study if the extra work required for applying the BEAD technique is worth it in terms of reduction of errors. The WLAP technique has therefore been applied to the TWP-ICE CPI data and the fractional differences with the CSI IWCs has been calculated over the IWC range. The fractional differences obtained using the WLAP and BEAD techniques on the same data sample are given in Fig. 11c. This sample is not exactly the same as when the BEAD technique was applied in Figs. 11a,b, hence the small difference in the

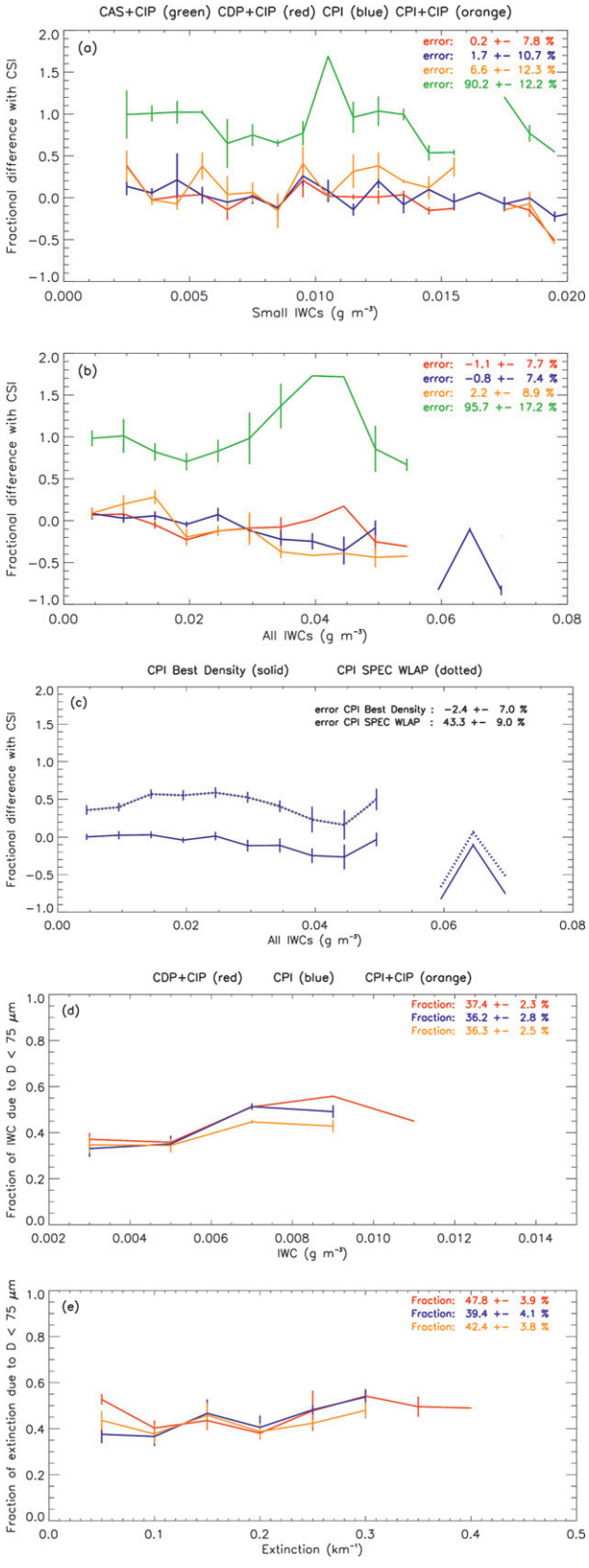

error statistics. From this figure, it is obtained that the BEAD and WLAP techniques are characterized by roughly the same standard deviation of the error (around 7%–9%), which shows that both estimates are robust. However, the BEAD technique produces a very small bias (−2.4%), while the WLAP technique overestimates the CSI IWCs by 43%. It seems therefore that the particle habit classification is required for the type of cirrus clouds sampled during TWP-ICE to produce the best IWC estimates from the particle size distributions. It will be very interesting in the future to compare the two techniques again in other environmental conditions to evaluate if this conclusion still holds.

A similar error analysis is carried out to quantify the value of the BEAD technique as compared with the use of single ρ–D relationships. It must be noted here again that the practice of using a single ρ–D relationship in such calculations is common for the derivation of IWC from in situ measurements and as an implicit assumption in active remote sensing retrievals of ice cloud properties. The result of this error analysis is reported for aggregates (Fig. 12a), bullet rosettes (Fig. 12b), hexagonal plates (Fig. 12c), and hexagonal columns (Fig. 12d). As seen from a comparison with Fig. 11b, the use of these four single ρ–D relationships produces either large positive or negative mean fractional differences, and none produces as small of a bias as the BEAD technique. The use of aggregates results in a bias of 68%–80% depending on the sensor combination, with a significant increase of the standard deviation over the calculations using the BEAD technique. There is also a degradation of the agreement for small IWCs (up to a factor of 2). The three other particle habits produce a relatively large negative bias (around −50% for bullet rosettes and hexagonal plates, and from around −25% to −20% for hexagonal columns), but a similar or slightly smaller standard deviation of the fractional difference when compared to the BEAD technique (Fig. 11). This negative bias is virtually constant over the IWC range for bullet rosettes and

←

FIG. 11. Fractional difference in IWC with respect to CSI as a function of IWC when using CAS + CIP (green), CDP + CIP (red), CPI + CIP (orange), and CPI alone (blue) for (a) the IWCs < 0.02 g m^{-3} and (b) the whole IWC range. For these calculations the BEAD technique has been used (see text for explanation). (c) Comparison of the fractional differences in IWC with respect to CSI produced by the BEAD and WLAP techniques, using the CPI data. Fraction of (d) IWC and (e) visible extinction produced by the particles with $D < 75$ μm in IWC and visible extinction bins. In all panels, error bars represent the standard deviation of the fractional difference in each IWC bin. Mean bias and standard deviation are also given as numbers for all combinations. Note that the CPI $N(D)$ have been multiplied by 4 to produce these results.

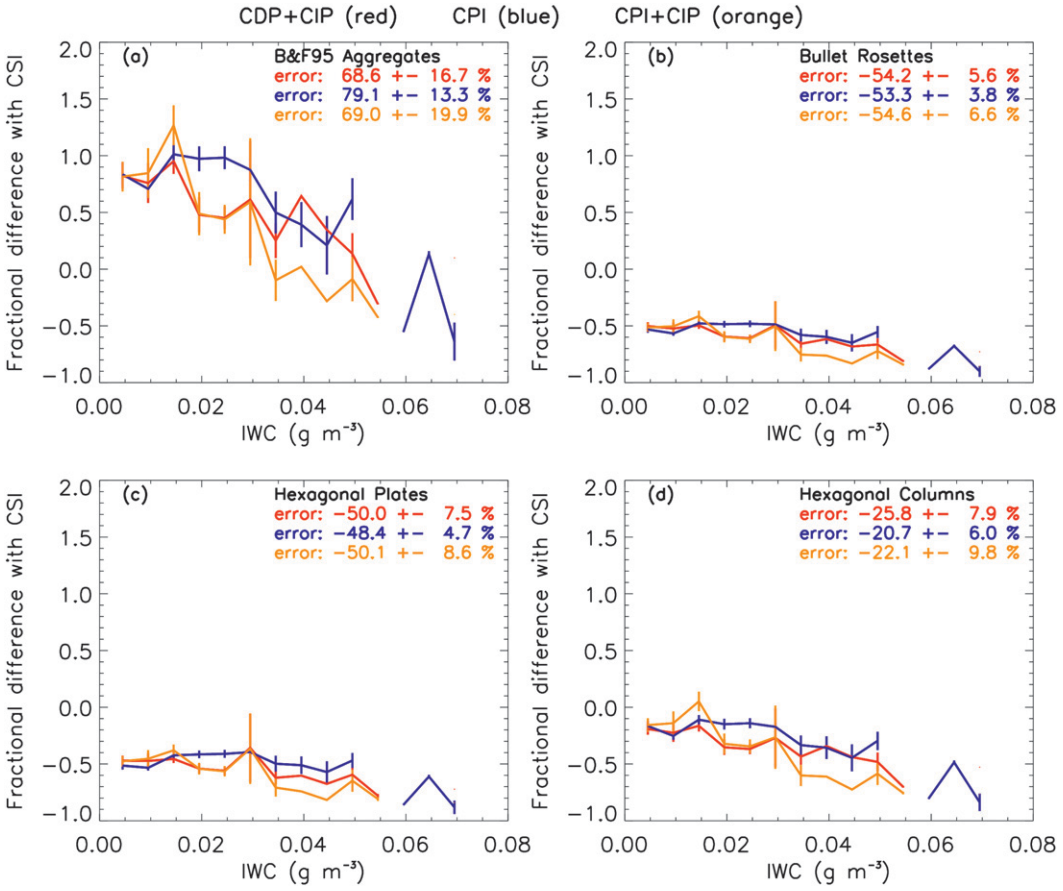

FIG. 12. Fractional difference in IWC with respect to CSI as a function of IWC when using CDP + CIP (red), CPI + CIP (orange), and CPI alone (blue) and using different ρ–D assumptions: (a) the Brown and Francis (1995) aggregates, (b) the Mitchell (1996) bullet rosettes, (c) the Mitchell (1996) hexagonal plates, and (d) the Mitchell (1996) hexagonal columns. Error bars represent the standard deviation of the fractional difference in each bin. Mean bias and standard deviation are also given as numbers for all combinations. Note that the CPI $N(D)$ have been multiplied by 4.

hexagonal plates. In contrast the negative bias for the hexagonal columns gets larger for the larger IWCs. Overall, the comparison of Figs. 11 and 12 highlights the value of using the CPI classification and the BEAD technique described in section 5 to calculate unbiased estimates of IWC from particle size distributions.

For visible extinction, total number concentration (N_T), and effective radius (R_{EFF}) there is no reference measurement to conduct an error analysis. However, for each flight segment the combinations validated according to the IWC criteria (systematically excluding the CAS + CIP combination) were used to compute these parameters. When two or more probe combinations are validated for a given time period, a mean value [e.g., for any cloud parameter C: $(1/N)\sum_{i=1}^{N} C(i)$, where N is the number of validated probe combinations] and a maximum difference (e.g., for three validated probe combinations: max{abs[$C(1) - C(2)$], abs[$C(2) - C(3)$], abs[$C(1) - C(3)$]} are calculated from the validated probe combinations. The ratio of the maximum difference to the mean value gives a fractional difference, interpreted as the error on the bulk microphysical property due to uncertainties in the $N(D)$ measurements. Means and standard deviations of these fractional differences are displayed in Fig. 13. For visible extinction (Fig. 13a), the mean fractional difference is around 33%, with a standard deviation of 7%. This larger fractional difference produced by different $N(D)$ measurements reflects the greater dependency of extinction to the $N(D)$ of small ice particles relative to that of IWC (because these small particles make greater contributions to extinction than to IWC). Despite the larger variability, extinction estimates with a 30% uncertainty are useful for the evaluation of ground-based radar–lidar retrievals. The mean fractional difference for R_{EFF} (Fig. 13b) is 21%, with a standard deviation of 5%. This fractional

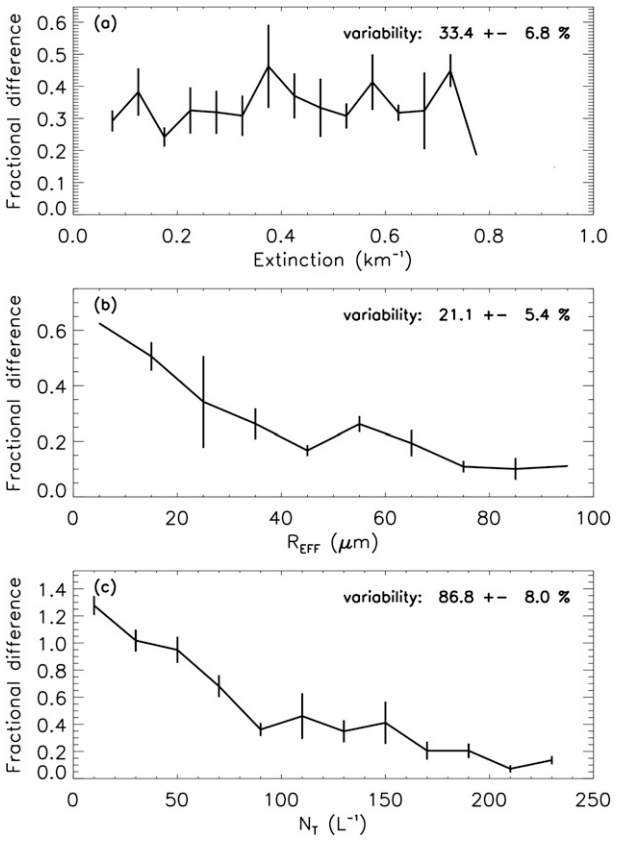

FIG. 13. Binned fractional difference of (a) visible extinction, (b) total concentration N_T, and (c) effective radius R_{EFF} derived from the variability between the estimates from the different combinations. Error bars represent the standard deviation of the fractional difference in each bin. The mean and standard deviation of these fractional differences are also given as numbers in the panels.

difference varies a lot over the R_{EFF} range, decreasing linearly from 60% to 20% from 5 to 40 μm and fluctuating around 10%–20% for R_{EFF} larger than 40 μm. The largest mean variability is found for N_T (Fig. 13c), which was expected given the large differences in the particle size distributions of small particles, the main contributors to total number concentration. However, this variability is not constant over the N_T range. For $N_T < 40$ L^{-1}, the different estimates vary by larger than a factor of 2, but decrease rapidly to 40% for $N_T =$ 100 L^{-1}, and even smaller for $N_T > 150$ L^{-1} (10%–20%). Therefore, caution should be exercised when using the N_T derived in the present study for radar–lidar retrieval evaluation for $N_T < 60$–80 L^{-1}. Larger values are most likely of better accuracy than the radar–lidar retrievals of total concentration, since the radar–lidar estimates of this quantity are very indirect and presumably prone to large errors, though this is yet to be quantified.

c. *The contribution of the small ice crystals to IWC and extinction*

Given the recently identified problem with shattering of large ice crystals on the tips of microphysical probes, it is anticipated that the contribution of small ice crystals to the bulk microphysical properties of clouds has been overestimated so far in the literature. This has been recently addressed for tropical anvil cirrus by Jensen et al. (2009) who indeed found that crystals of maximum dimension smaller than 55 μm contributed very little to cloud extinction and radiative properties. However, their TC4 dataset includes much larger IWCs and extinctions than during TWP-ICE. This is probably due to the fact that the TC4 flights were systematically at lower heights into the anvil (from 9- to 12-km height), as compared with the high-altitude flights during TWP-ICE (from 12- to 16-km height). As a result, it is expected that anvil regions where aggregation and sublimation are the dominant processes were sampled during TC4, while the TWP-ICE measurements were more representative of the upper cloud portion where crystal growth is realized through water vapor deposition (and probably some aggregation too), with fewer large crystals and presumably a larger contribution of small crystals to the bulk microphysical properties.

The contribution of crystals of maximum dimension smaller than 75 μm to the cloud IWC and extinction is calculated as the fraction of IWC and extinction produced by these small crystals to the total IWC and extinction. The results are reported in Fig. 11d for IWC and Fig. 11e for visible extinction. From these figures it is clearly observed that the contribution of small crystals is much larger than that found in Jensen et al. (2009). The contribution of small crystals to IWC is 36%–37%, and this contribution varies very little with the chosen probe combination (Fig. 11d). The contribution of small crystals to visible extinction is slightly larger (Fig. 11e), and the estimate of this contribution ranges from 40% to 47% depending on the probe combination considered, the largest differences between probes being found for visible extinctions smaller than 0.1 km^{-1}. This contribution of small crystals to IWC and cloud extinction is relatively constant (from 35% to 50% for IWC and from 40% to 55% for extinction) over the IWC and extinction ranges sampled during TWP-ICE. These numbers are much larger than those reported by Jensen et al. (2009), which is as discussed previously probably due to the fact that different growth regions with different dominant microphysical processes have been sampled during TC4 and TWP-ICE. This contribution of small ice crystals is, however, much lower than what has been reported in the literature using probe measurements significantly

contaminated by shattered particles [see, e.g., numbers obtained by McFarquhar et al. (2007a) with the CAS + CIP combination in TWP-ICE].

7. Summary and conclusions

In this study, the bulk microphysical properties of two cases of aged cirrus clouds (the 27/01 and 29/01 cases), and a fresh anvil produced by deep convective activity over the Tiwi Islands (the 02/02 case) observed during TWP-ICE are estimated. Consistent with earlier studies, small ice particles with maximum dimensions $D <$ 100 μm are predominantly quasi-spherical, with the degree of nonsphericity increasing rapidly in the $50 < D <$ 100-μm range. For $D > 100$ μm, the CPI particle habit classification varies between the three flights. The aged cirrus clouds are predominantly characterized by bullet rosettes and aggregates of bullet rosettes, plates, and columns. In contrast, the fresh anvil is associated with much larger occurrences of pristine habits such as plates, columns, aggregates of plates, and occasionally capped columns.

The overlap in size ranges of the different in situ microphysical sensors used during TWP-ICE was exploited to assess the quality of the observations, detect systematic and intermittent problems with the sensors, estimate the possible contamination by the shattering of large particles on the probe tips, and estimate an unknown scaling factor for the CPI. The study of the correlation between the total concentration of small ice crystals and the ice water content as measured by the CSI revealed that the impact of shattering is probably small for the CPI and CDP probes, and very large for the CAS. For the 27/01 and 29/01 flights, the CAS $N(D)$ were found to be 7 and 30 times greater than the CDP $N(D)$ and 9 and 40 times greater than the CPI $N(D)$ respectively for 27/01 and 29/01. The suggested small contribution of shattering to the CPI measurements is also confirmed by the analysis of the number of particles per CPI frame, showing that more than 98% of the CPI frames include only one particle, and that the number of particles per frame does not depend on the concentration of large crystals.

Then, using the CIP measurements for $D \geq 100$ μm as a reference, it has been shown that the correlation between the CPI and CIP measurements in that range was high (0.78), but that CPI $N(D)$ were underestimated by a factor of 4. This factor of 4 was applied as a scaling factor for subsequent calculations. It was also shown that the $N(D)$ measured in the first bins of the CIP (50 and 75 μm) were in good agreement with these scaled CPI $N(D)$, although large errors were expected for the CIP measurements for these first bins because of undersizing of larger particles due to different well-known uncertainties in these measurements. These bins have therefore been included in the CDP CIP probe combination. In contrast the CDP and CPI measurements for $D < 50$ μm were not found to be correlated at all, which implies that something is wrong with one of those measurements. The TWP-ICE data cannot be analyzed further to determine which probe is wrong.

A methodology to reduce errors associated with the ρ–D and A–D assumptions in bulk microphysics calculations was developed using particle habit classification from the CPI and applied to the three TWP-ICE flights. This method (named BEAD) makes use of the frequency of occurrence of each particle habit and prescribed ρ–D and A–D relationships from Brown and Francis (1995) and Mitchell (1996). This approach produced much better agreement with the CSI IWCs than the use of a single particle habit ρ–D relationship, no matter which habit was considered. The BEAD method has also been compared with a well-established technique called WLAP (Baker and Lawson 2006). It has been shown that the BEAD and WLAP methods produced a similar standard deviation of the error, but the WLAP was characterized by a larger bias of 40% as compared with a very small bias for the BEAD method when using the TWP-ICE dataset. Recent field experiments including bulk measurements in addition to IWC (i.e. extinction, radar reflectivity) will be investigated in the future to get a more comprehensive analysis of the improvement brought to the estimates of the bulk microphysical properties with this BEAD technique.

The impact of the large differences in particle size distributions measured by four combinations of sensors (CAS + CIP, CDP + CIP, CPI alone, CPI + CIP) on the resulting bulk microphysical properties was characterized both from individual time series and statistically. Using the bulk IWC from the CSI as a reference, the errors on derived IWC were estimated. The contribution of small ice crystals (less than 75 μm in maximum dimension) to IWC and visible extinction has been quantified. It is of the order of 37% for IWC and 40%–47% for visible extinction. This is different from the findings in Jensen et al. (2009), who found a much smaller contribution. This difference is attributed to the fact that the TWP-ICE data are more representative of the upper levels in tropical anvil cirrus.

The mean fractional differences were found to be small for the CPI + CIP, CPI, and CDP + CIP combinations (2.2%, −0.8%, and −1.1%, respectively), with standard deviations of the fractional differences ranging from 7% to 9%. This magnitude of errors is compatible with using those estimates as references for radar–lidar cloud retrievals. The CAS + CIP combination produces

a mean and a standard deviation of the fractional difference of 95% and 17%, respectively. The good agreement of the CSI IWC and the IWCs estimated from the corrected CPI concentrations provides an independent validation of the CPI scaling factor. The analysis of the variability between the different estimates of extinction, R_{EFF}, and N_T produced mean fractional differences of 33% for extinction, 21% for R_{EFF}, and 87% for N_T, with relatively small standard deviations of 5%–8%. For extinction, the fractional difference is similar over the whole extinction range. This is not the case for R_{EFF} and N_T, for which errors are much larger for small values. The largest variability is found for N_T. For $N_T < 40\ \mathrm{L}^{-1}$, the different estimates vary by larger than a factor of 2, but decrease rapidly to 40% for $N_T = 100\ \mathrm{L}^{-1}$, and even smaller for $N_T > 150\ \mathrm{L}^{-1}$ (10%–20%). Therefore, caution should be exercised when using the N_T derived in the present study for radar–lidar retrieval evaluation for $N_T < 60$–$80\ \mathrm{L}^{-1}$.

More state-of-the-art in situ microphysical observations (with shattering removed as in TC4) in different regions of the world are needed to confirm some of the findings of this study. More direct bulk measurements of the cloud microphysical properties are also needed to better constrain the methodology employed in this study (lidar extinction, radar reflectivity and crystal fall speed, and direct in situ measurements of visible extinction). This will be the subject of future investigations.

Acknowledgments. This work has been partly supported by the U.S. Department of Energy Atmospheric Radiation Measurement Program. The Darwin radar data were obtained from the Program. Archive. Peter May and Justin Peter from CAWCR are thanked for their comments on an earlier version of the manuscript.

APPENDIX

The ρ–D and A–D Relationships Used to Calculate Best Estimates of the Density and Projected Area in Each D Bin

From the original 11 habits used in the CPI particle habit classification four $\rho(D)$ classes and five $A(D)$ classes were derived for calculating the bulk microphysical properties. The smaller number of classes is due to the fact that some particle habits are characterized by the same ρD and/or the same A–D relationships in the literature.

The $\rho(D)$ classes are as follows:

ρ1—aggregates (QS) (Brown and Francis 1995):

$$D < 97\ \mu\mathrm{m} \quad \rho(D) = 0.917; \tag{A1}$$

$$D \geq 97\ \mu\mathrm{m} \quad \rho(D) = \frac{0.917}{D_l \times 10^4}(D \times 10^4)^{-1.1}, \quad D_l = 97\ \mu\mathrm{m}. \tag{A2}$$

ρ2—bullet rosettes and their aggregates (BR + ABR) (Mitchell 1996):

$$\rho(D) = 0.005\,88(D \times 10^4)^{-0.74}. \tag{A3}$$

ρ3—plates and their aggregates (PLT + AP) (Mitchell 1996):

$$\rho(D) = 0.014\,113\,86(D \times 10^4)^{-0.55}. \tag{A4}$$

ρ4—columns, capped columns, and their aggregates (COL + CC+ AC) (Mitchell 1996):

$$D < 100\ \mu\mathrm{m} \quad \rho(D) = 0.320\,283\,41(D \times 10^4)^{-0.09}; \tag{A5}$$

$$100 < D < 300\ \mu\mathrm{m} \quad \rho(D) = 0.0317(D \times 10^4)^{-1.0}; \tag{A6}$$

$$D > 300\ \mu\mathrm{m} \quad \rho(D) = 0.001\,732\,24(D \times 10^4)^{-1.26}, \tag{A7}$$

with $\rho(D)$ in grams per centimeter cubed and D in micrometers.

The $A(D)$ classes are as follows:

A1—spheres (QS):

$$A(D) = \frac{\pi(D \times 10^4)^2}{4}. \tag{A8}$$

A2—bullet rosettes (BR) (Mitchell 1996):

$$A(D) = 0.0869(D \times 10^4)^{1.57}. \tag{A9}$$

A3—plates (PLT) (Mitchell 1996):

$$A(D) = 0.65(D \times 10^4)^2. \tag{A10}$$

A4—all aggregates (AP, AC, ABR, CC) (Mitchell 1996):

$$A(D) = 0.2285(D \times 10^4)^{1.88}. \tag{A11}$$

A5—columns (COL) (Mitchell 1996):

$$D < 100\ \mu\text{m}$$

$$A(D) = 0.684(D \times 10^4)^2; \qquad \text{(A12)}$$

$$100 < D < 300\ \mu\text{m}$$

$$A(D) = 0.0696(D \times 10^4)^{1.5}; \qquad \text{(A13)}$$

$$D > 300\ \mu\text{m}$$

$$A(D) = 0.0512(D \times 10^4)^{1.414}, \qquad \text{(A14)}$$

with A(D) in centimeters squared and D in micrometers.

REFERENCES

Baker, B., and R. P. Lawson, 2006: Improvement in determination of ice water content from two-dimensional particle imagery. Part I: Image-to-mass relationships. *J. Appl. Meteor. Climatol.,* **45,** 1282–1290.

Baumgardner, D., and A. Korolev, 1997: Airspeed corrections for optical array probe sample volumes. *J. Atmos. Oceanic Technol.,* **14,** 1224–1229.

Bony, S., and Coauthors, 2006: How well do we understand and evaluate climate change feedback processes? *J. Climate,* **19,** 3445–3482.

Brown, P. R. A., and P. N. Francis, 1995: Improved measurements of the ice water content in cirrus using a total-water probe. *J. Atmos. Oceanic Technol.,* **12,** 410–414.

Connolly, P. J., M. J. Flynn, Z. Ulanowski, T. W. Choularton, M. W. Gallagher, and K. N. Bower, 2007: Calibration of the cloud particle imager probes using calibration beads and ice crystal analogs: The depth of field. *J. Atmos. Oceanic Technol.,* **24,** 1860–1879.

Delanoë, J., A. Protat, J. Testud, D. Bouniol, A. J. Heymsfield, A. Bansemer, P. R. A. Brown, and R. M. Forbes, 2005: Statistical properties of the normalized ice particle size distribution. *J. Geophys. Res.,* **110,** D10201, doi:10.1029/2004JD005405.

Dufresne, J.-L., and S. Bony, 2008: An assessment of the primary sources of spread of global warming estimates from coupled atmosphere–ocean models. *J. Climate,* **21,** 5135–5144.

Field, P. R., R. Wood, P. R. A. Brown, P. H. Kaye, E. Hirst, R. Greenaway, and J. A. Smith, 2003: Ice particle interarrival times measured with a fast FSSP. *J. Atmos. Oceanic Technol.,* **20,** 249–261.

——, A. J. Heymsfield, and A. Bansemer, 2006: Shattering and particle interarrival times measured by optical array probes in ice clouds. *J. Atmos. Oceanic Technol.,* **23,** 1357–1371.

Heymsfield, A. J., 2007: On measurements of small ice particles in clouds. *Geophys. Res. Lett.,* **34,** L23812, doi:10.1029/2007GL030951.

——, C. Schmitt, A. Bansemer, G.-J. van Zadelhoff, M. J. McGill, C. Twohy, and D. Baumgardner, 2006: Effective radius of ice cloud particle populations derived from aircraft probes. *J. Atmos. Oceanic Technol.,* **23,** 361–380.

——, A. Bansemer, and C. Twohy, 2007: Refinements to ice particle mass dimensional and terminal velocity relationships for ice clouds. Part I: Temperature dependence. *J. Atmos. Sci.,* **64,** 1047–1067.

Jakob, C., 2002: Ice clouds in numerical weather prediction models: Progress, problems and prospects. *Cirrus,* D. Lynch et al., Eds., Oxford University Press, 327–345.

Jensen, E. J., and Coauthors, 2009: On the importance of small ice crystals in tropical anvil cirrus. *Atmos. Chem. Phys.,* **9,** 5519–5537.

Korolev, A., 2007: Reconstruction of the sizes of spherical particles from their shadow images. Part I: Theoretical considerations. *J. Atmos. Oceanic Technol.,* **24,** 376–389.

——, and G. A. Isaac, 2005: Shattering during sampling by OAPs and HVPS. Part I: Snow particles. *J. Atmos. Oceanic Technol.,* **22,** 528–542.

——, J. W. Strapp, and G. A. Isaac, 1998: Evaluation of the accuracy of PMS optical array probes. *J. Atmos. Oceanic Technol.,* **15,** 708–720.

Lawson, R. P., D. O'Connor, P. Zmarzly, K. Weaver, B. A. Baker, Q. Mo, and H. Jonsson, 2006: The 2D-S (Stereo) probe: Design and preliminary tests of a new airborne, high-speed, high-resolution imaging probe. *J. Atmos. Oceanic Technol.,* **23,** 1462–1477.

Mather, J. H., S. A. McFarlane, M. A. Miller, and K. L. Johnson, 2007: Cloud properties and associated radiative heating rates in the tropical western Pacific. *J. Geophys. Res.,* **112,** D05201, doi:10.1029/2006JD007555.

May, P. T., J. H. Mather, G. Vaughan, C. Jakob, G. M. McFarquhar, K. N. Bower, and G. G. Mace, 2008: The Tropical Warm Pool International Cloud Experiment. *Bull. Amer. Meteor. Soc.,* **89,** 629–645.

McFarquhar, G. M., and S. G. Cober, 2004: Single-scattering properties of mixed-phase Arctic clouds at solar wavelengths: Impacts on radiative transfer. *J. Climate,* **17,** 3799–3813.

——, P. Yang, A. Macke, and A. J. Baran, 2002: A new parameterization of single-scattering solar radiative properties for tropical ice clouds using observed ice crystal size and shape distributions. *J. Atmos. Sci.,* **59,** 2458–2478.

——, J. Um, M. Freer, D. Baumgardner, G. L. Kok, and G. Mace, 2007a: Importance of small ice crystals to cirrus properties: Observations from the Tropical Warm Pool International Cloud Experiment (TWP-ICE). *Geophys. Res. Lett.,* **34,** L13803, doi:10.1029/2007GL029865.

——, G. Zhang, M. R. Poellot, G. L. Kok, R. McCoy, T. Tooman, A. Fridlind, and A. J. Heymsfield, 2007b: Ice properties of single-layer stratocumulus during the Mixed-Phase Arctic Cloud Experiment: 1. Observations. *J. Geophys. Res.,* **112,** D24201, doi:10.1029/2007JD008633.

Mioche, G., D. Josset, J.-F. Gayet, J. Pelon, A. Garnier, A. Minikin, and A. Schwarzenboeck, 2010: Validation of the *CALIPSO*–CALIOP extinction coefficients from in situ observations in midlatitude cirrus clouds during CIRCLE-2 experiment. *J. Geophys. Res.,* **115,** D00H25, doi:10.1029/2009JD012376.

Mitchell, D. L., 1996: Use of mass- and area-dimensional power laws for determining precipitation particle terminal velocities. *J. Atmos. Sci.,* **53,** 1710–1723.

Sassen, K., Z. Wang, and D. Liu, 2008: Global distribution of cirrus clouds from *CloudSat*/*Cloud-Aerosol Lidar and Infrared Pathfinder Satellite Observations* (*CALIPSO*) measurements. *J. Geophys. Res.,* **113,** D00A12, doi:10.1029/2008JD009972.

Stephens, G. L., S.-C. Tsay, P. W. Stackhouse, and P. J. Flatau, 1990: The relevance of the microphysical and radiative properties of cirrus clouds to climate and climatic feedback. *J. Atmos. Sci.,* **47,** 1742–1754.

——, and Coauthors, 2002: The *CloudSat* mission and the A-Train: A new dimension of space-based observations of

clouds and precipitation. *Bull. Amer. Meteor. Soc.,* **83,** 1771–1790.

Stokes, G. M., and S. E. Schwartz, 1994: The Atmospheric Radiation Measurement (ARM) Program: Programmatic background and design of the Cloud and Radiation Test Bed. *Bull. Amer. Meteor. Soc.,* **75,** 1201–1221.

Strapp, J. W., F. Albers, A. Reuter, A. V. Korolev, U. Maixner, E. Rashke, and Z. Vukovic, 2001: Laboratory measurements of the response of a PMS OAP-2DC. *J. Atmos. Oceanic Technol.,* **18,** 1150–1170.

Tian, L., G. M. Heymsfield, L. Li, A. J. Heymsfield, A. Bansemer, C. H. Twohy, and R. C. Srivastava, 2010: A study of cirrus ice particle size distribution using TC4 observations. *J. Atmos. Sci.,* **67,** 195–216.

Twohy, C. H., J. W. Strapp, and M. Wendisch, 2003: Performance of a counterflow virtual impactor in the NASA icing research tunnel. *J. Atmos. Oceanic Technol.,* **20,** 781–790.

Ulanowski, Z., P. J. Connolly, M. J. Flynn, M. W. Gallagher, A. J. M. Clarke, and E. Hesse, 2004: Using ice crystal analogues to validate cloud ice parameter retrievals from the CPI ice spectrometer data. *Proc. 14th Int. Conf. on Clouds and Precipitation,* Bologna, Italy, WMO, 1–4.

Um, J., and G. M. McFarquhar, 2007: Single-scattering properties of aggregates of bullet rosettes in cirrus. *J. Appl. Meteor. Climatol.,* **46,** 757–775.

——, and ——, 2009: Single-scattering properties of aggregates of plates from TWP-ICE. *Quart. J. Roy. Meteor. Soc.,* **135,** 291–304.